# Kinetic Zr isotope fractionation on Mars recorded in ancient Zr-rich minerals

**N.K. Jensen, M.M. Costa, Z. Deng, J.N. Connelly, M. Bizzarro**

## Supplementary Information

The Supplementary Information includes:



## Materials and Methods

### Zircon and baddeleyite from NWA 7533

The majority (21 out of 26) of the zircon and baddeleyite grains used in this project were separated from a crushed bulk aliquot of the martian regolith breccia meteorite as part of a previous project (Costa *et al.*, 2020). These grains typically have a brown, granular and/or cloudy appearance indicating fracturing, metamictisation (*i.e.* the formation of amorphous zones within the crystals due to radiation damage from the decay of U), and/or shock metamorphism (*e.g.*, the formation of neoblastic crystallites, Cavosie *et al.*, 2018). Since the previous project was aimed at obtaining high-precision age constraints for early crust formation on Mars, these grains were not selected for analysis. Instead, the 21 grains were picked for this study. Whereas disturbed U-Pb isotope systematics are expected given that Pb is readily lost from damaged domains in the crystal, the brown/granular grains might preserve pristine Hf and Zr isotope compositions due to the slow diffusion of these elements in the zircon crystal lattice (Cherniak *et al.*, 1997), and the immobile behaviour of the high field strength elements (HFSEs, incl. Zr and Hf) during secondary alteration processes (with some exceptions, see Jiang *et al.*, 2005). We note that elements traditionally considered immobile in zircon could diffuse faster in amorphous zones (*e.g.*, Geisler *et al.*, 2002). As such, it is necessary to assess the level of isotope disturbance in the grains of this study, which is permitted through the concomitant determination of the U-Pb, Lu-Hf and stable Zr isotope compositions. In detail, potential Lu-Hf isotope disturbance can be evaluated by comparison of the isotope compositions to that previously reported for pristine NWA 7533 zircons (see Fig. S-9). Further, the stable Zr isotope compositions

can be compared to the level of U-Pb isotope discordance recorded in the grains to assess whether the U-Pb disturbance event also modified the Zr isotope signatures (see Fig. S-6a).

In addition to the 21 grains separated from the bulk NWA 7533 breccia, we analysed the Zr isotope compositions of five zircons that were previously separated from the basaltic andesitic NWA 7533 clast C28 and measured for their U-Pb and Lu-Hf isotope compositions (for details, refer to Jensen *et al.*, 2025b). A detailed description of the zircon/baddeleyite separation method is provided in Costa *et al.* (2020) and Jensen *et al.* (2025b). It should be emphasised that the separation of zircons from NWA 7533 is a very time-consuming task and that the zircon/baddeleyite grains are typically too small for physical manipulation and analysis. Given the limited mass of NWA 7533 available for study, separating additional well-preserved (non-metamict) grains was not considered feasible at the time of this project.

**Sample imaging**

Prior to digestion, the zircon and baddeleyite grains used in this study were spread out and adhered to a glass slide in a sugar-water mixture in preparation for imaging by scanning electron microscopy (SEM) using the ZEISS® EVO 15 SEM at the Centre for Star and Planet Formation, Copenhagen. The SEM, equipped with a lanthanum hexaboride electron source and a Bruker XFlash® 6|30 EDS detector, was operated in variable pressure mode (~30 Pa) to reduce charging effects and devolatilisation of the sugar-substrate. Backscattered electron (BSE) images of the selected zircon and baddeleyite grains were typically captured with a target current of 1.85 A, 12 kV accelerating voltage, and 600 pA beam current at a working distance of ~8.5 mm. The mineralogy of the imaged grains was identified based on EDX spectra. We refer to Figures S-1 to S-3 for BSE images (on sugar substrate) and optical light images (in ethanol) of the zircon and baddeleyite grains separated from the crushed bulk aliquot of NWA 7533, and to Figures S-8 to S-10 in Jensen *et al.* (2025b) for images of the five U-Pb-dated zircons from the basaltic andesitic clast C28.

**Sample digestion**

The procedure for zircon and baddeleyite digestion follows low-Pb-blank methods that have been described in detail in earlier publications (Bouvier *et al.*, 2018; Costa *et al.*, 2020). Prior to digestion, the zircon and baddeleyite grains were cleaned in alternate steps of warm 3.5 M $HNO_3$, distilled $H_2O$ (two times), and twice-distilled acetone (two times) in an ultrasonic bath. Zircon grains with a granular and dark brown appearance were subjected to an additional cleaning step using warm 6 M HCl preceding the $H_2O$ step. Then, the grains were digested individually in Krogh-type Teflon™ bombs in a 3:1 mixture of 28 M HF and 7 M $HNO_3$ in an oven at 210 °C for at least four days together with the mixed $^{202}Pb$-$^{205}Pb$-$^{233}U$-$^{235}U$ EARTHTIME tracer (Condon *et al.*, 2015; McLean *et al.*, 2015). After evaporation to dryness, and in preparation for U-Pb chromatography, the samples were dissolved overnight in 3.1 M HCl in the oven at 180 °C.

**Spiking and ion exchange chromatography**

The methods for concomitant determination of the stable Zr, Lu-Hf and U-Pb isotope compositions of small zircon and baddeleyite, involving the addition of a Zr double spike that has been purified from Hf, are described in detail in Jensen *et al.* (2024). The main steps are summarised below.

The zircon and baddeleyite digestions were processed through a four-step chromatographic separation, with the first step aimed at U-Pb separation following a well-established low-contamination method modified after Krogh (1973). The samples, dissolved in 3.1 M HCl, were loaded onto miniature heat-shrink Teflon™ columns with pre-cleaned AG1-X8 resin (200-400 mesh). The zircon matrix elements (Zr, Hf, REEs ± Ti) were eluted with 3.1 M HCl, followed by U and Pb elution with 6 M HCl and $H_2O$. One drop (8 µl) of phosphoric acid (0.1 M $H_3PO_4$) was added to the U-Pb cuts, followed by evaporation to dryness in preparation for mass spectrometry.

Prior to further purification, the matrix cuts from the U-Pb chemistry were split in two, saving 5-10 % aliquots (depending on the sample size) for Lu/Hf and Zr/Hf ratio determination. The remaining 90-95 % aliquots (although,

maximum 200-ng Zr aliquots) were equilibrated with the purified Zr double spike and processed through three additional chromatographic purification steps to separate Zr from Hf (on TEVA-spec resin, 100-150 µm), purify Hf from Ti (DGA resin, 50-100 µm) and, finally, remove any Mo introduced to the Zr cuts through the chemical procedure (AG1-X8 resin, 100-200 mesh). The purified Zr and Hf cuts and the 5-10 % aliquots for element ratio determination were evaporated to dryness and re-dissolved in 0.5 M $HNO_3$-0.01 M HF in preparation for mass spectrometry.

For each of the two largest zircons (NS5b2 and NS5b3), we processed an extra 200-ng Zr aliquot for Hf isotope measurements without the addition of Zr double spike. The $^{176}Hf/^{177}Hf$ and $^{178}Hf/^{177}Hf$ results for these unspiked aliquots are within uncertainty of the two aliquots processed with Zr double spike, confirming the conclusions in Jensen *et al.* (2024) that the addition of the purified Zr double spike does not lead to a discernible bias on the $^{176}Hf/^{177}Hf$ and $^{178}Hf/^{177}Hf$ ratios (Table S-1).

**Table S-1** Hf isotope results for Zr double-spiked and unspiked ~3.5-ng Hf aliquots of NWA 7533 zircons.

| | $^{176}Hf/^{177}Hf$ | $^{178}Hf/^{177}Hf$ | $^{180}Hf/^{177}Hf$ | εHf at T |
|---|---|---|---|---|
| *Spiked aliquots* | | | | |
| NS5b2 | 0.279921 ± 12 | 1.46718 ± 2 | 1.88728 ± 5 | -6.1 ± 0.7 |
| NS5b3 | 0.279911 ± 13 | 1.46717 ± 2 | 1.88715 ± 6 | -5.5 ± 0.7 |
| *Unspiked zircon aliquots* | | | | |
| NS5b2 | 0.279932 ± 11 | 1.46716 ± 3 | 1.88664 ± 8 | -5.7 ± 0.7 |
| NS5b3 | 0.279903 ± 12 | 1.46717 ± 2 | 1.88661 ± 5 | -5.8 ± 0.7 |
| *Deviation (ppm)* | | | | |
| NS5b2 | -39 ± 82 | 13 ± 33 | 339 ± 73 | |
| NS5b3 | 29 ± 89 | 3 ± 29 | 286 ± 59 | |

Uncertainties on the Hf isotope ratios reflect the 2SE internal precision in the last decimal places.
Note that the uncertainties on the εHf values are identical because they are calculated by propagating the external reproducibility.
The uncertainties on the ppm-deviations are calculated using the internal uncertainties reported for the isotope ratios.
T refers to the $^{207}Pb/^{206}Pb$ date measured for the sample.

## Mass spectrometry

***Zirconium isotope measurements.*** The Zr isotope measurements were conducted on a Thermo Scientific™ Neptune Plus multi-collector (MC-)ICPMS at the Centre for Star and Planet Formation, Copenhagen, and followed the method described in detail in Jensen *et al.* (2024). In brief, the purified Zr cuts were aspirated into the plasma source in 0.5 M $HNO_3$-0.01 M HF using an Apex HF desolvating nebuliser, and the Zr isotope masses (90, 91, 92, 94, 96), $^{95}Mo$, $^{98}Mo$, and $^{99}Ru$ were collected simultaneously in Faraday cups connected to $10^{11}$ Ω amplifiers, except for $^{95}Mo$ and $^{98}Mo$ for which $10^{13}$ Ω amplifiers were used. Sample analyses were interspaced with analyses of the baseline as well as the IPGP-Zr reference material (obtained from IPGP) spiked with a batch of $^{91}Zr$-$^{96}Zr$ double spike that has been purified for Hf (Jensen *et al.*, 2024). Due to the different sizes of zircon and baddeleyite grains, the length of the sample measurements varied between a single block of ≤50 cycles (8.39 s integration time), and up to 5 blocks of 50 cycles for the largest samples containing 200 ng Zr. The smallest samples that were only measured once were interspaced with an additional standard analysis. The employed method yields an estimated reproducibility of 0.015 ‰ for samples containing 200 ng Zr, and 0.027 ‰ for small samples containing only 25 ng Zr in total. To the results we assign an external reproducibility of 0.015 ‰ in the case of samples that were measured more than one time (typically >60 ng Zr), and 0.027 ‰ in the case of samples that were measured only once (<60 ng Zr).

The Zr isotope data were processed using the Iolite data reduction software (Paton *et al.*, 2011) and the IsoSpike script for double-spike deconvolution (Creech and Paul, 2015). The isobaric interferences of $^{94,96}Mo$ on $^{94\text{-}96}Zr$ were corrected for using $^{95}Mo$ and the mass bias determined for Zr. The three baseline-subtracted and interference-corrected isotope ratios $^{91}Zr/^{90}Zr$, $^{94}Zr/^{90}Zr$ and $^{96}Zr/^{90}Zr$ were used for the double-spike deconvolution, and the stable Zr isotope data are

reported as the deviation of the sample $^{94}Zr/^{90}Zr$ ratio relative to that of the IPGP-Zr reference material in the per mil unit:

$$\delta^{94}Zr\ [‰] = \left[\frac{\left(^{94}Zr/^{90}Zr\right)_{sample}}{\left(^{94}Zr/^{90}Zr\right)_{IPGP-Zr}} - 1\right] \text{x } 10^3$$

Importantly, the method for double spike deconvolution using three isotope ratios assumes mass dependency between the isotopes in question. As such, any deviation from mass dependency (relative to the bracketing Zr standard) requires a correction to achieve unbiased $\delta^{94}Zr$ results. In consistence with the approach in Jensen *et al.* (2025a), the data obtained for martian mineral grains in this study have been corrected for the invariable mass-independent anomaly on $^{96}Zr$ of +30 ppm reported for meteoritic samples from Mars (Burkhardt *et al.*, 2021; Render *et al.*, 2022). The $\delta^{94}Zr$ data reported in this paper can, thus, be directly compared to data obtained for terrestrial samples (providing that the data are normalised to the same Zr reference material).

***Lutetium-hafnium isotope measurements.*** The Lu-Hf isotope analyses were conducted on the same mass spectrometer and with roughly the same setup as used for Zr isotope analysis, except that the Apex HF was replaced with a Cetac Aridus II desolvating nebuliser using Ar and $N_2$ sweep gases for sample aspiration. A detailed description of the protocol can be found in Jensen *et al.* (2024) and Jensen *et al.* (2025b).

The Hf isotope ratios of the purified Hf cuts were measured using a sample-standard bracketing approach, where the sample analyses were interspaced by analyses of the baseline and the JMC 475 Hf standard. All the Hf isotope masses (176, 177, 178, 179, 180) along with $^{171}Yb$, $^{173}Yb$, $^{175}Lu$ and $^{182}W$ were collected simultaneously in Faraday cups connected to $10^{11}$ Ω amplifiers, except for $^{173}Yb$ and $^{175}Lu$ for which $10^{13}$ Ω amplifiers were used. Samples were analysed once, and the total amount of consumed Hf was typically between 0.5 and 5 ng. The blank-subtracted and interference-corrected ($^{180}W$ on $^{180}Hf$, $^{176}Lu$ and $^{176}Yb$ on $^{176}Hf$) Hf isotope ratios were corrected for instrumental mass fractionation by internal normalisation to $^{179}Hf/^{177}Hf_{true} = 0.7325$ (Patchett and Tatsumoto, 1980) using an exponential mass fractionation law (Russell *et al.*, 1978). Finally, the mass bias corrected $^{176}Hf/^{177}Hf$, $^{178}Hf/^{177}Hf$ and $^{180}Hf/^{177}Hf$ ratios were normalised to the conventionally accepted values for the JMC 475 Hf standard of 0.282160, 1.46717 and 1.88666, respectively (Stevenson and Patchett, 1990; Blichert-Toft *et al.*, 1997; Vervoort and Blichert-Toft, 1999). We note that the $^{180}Hf/^{177}Hf$ ratios determined for the samples are biased towards higher values due to the addition of Zr double spike with trace amounts of Hf (with an anomalous $^{180}Hf/^{177}Hf$ ratio). Thus, the $^{180}Hf/^{177}Hf$ ratios reported for these samples should not be used to assess the quality of the data. We emphasise that our method, which includes the addition of purified Zr double spike, leads to unbiased $^{176}Hf/^{177}Hf$ and $^{178}Hf/^{177}Hf$ ratios as demonstrated in Jensen *et al.* (2024). The reproducibility on $^{176}Hf/^{177}Hf$ using this method is 0.64 ε and 1.7 ε (parts per ten thousand) for 2.5 ng and 0.56 ng analysed Hf, respectively (Jensen *et al.*, 2024). Thus, to the results we assign an external reproducibility of 0.64 ε and 1.7 ε in the case of samples containing >1 and <1 ng Hf, respectively.

The Lu/Hf ratios were determined on the 5-10 % aliquots of the matrix (Zr, Hf, REEs ±Ti) cuts from the U-Pb chemistry using an in-house natural zircon reference solution (G15-7, for details about this reference solution see Jensen *et al.*, 2025b) as bracketing standard. The $^{175}Lu$ beam was collected on the axial secondary electron multiplier while $^{177}Hf$ was collected simultaneously in the H2 Faraday cup connected to a $10^{11}$ Ω amplifier. Combining all sources of uncertainty, the reproducibility of $^{176}Lu/^{177}Hf$ determination using this method is estimated to 0.93 % (Jensen *et al.*, 2025b).

The zircon and baddeleyite Hf isotope compositions at the time corresponding to the $^{207}Pb/^{206}Pb$ age was calculated using a $\lambda^{176}Lu$ value of $1.867 \pm 0.008 \times 10^{-11}$ year$^{-1}$ (Söderlund *et al.*, 2004) and CHondritic Uniform Reservoir (CHUR) parameters of Bouvier *et al.* (2008). The uncertainties (internal precision or external reproducibility, whichever is the largest) associated with the measured Hf isotope composition and the Lu/Hf ratio determination are propagated in the

final uncertainty quoted for the initial Hf isotope composition. The back-calculated Hf isotope compositions are reported as the parts-per-ten-thousand deviation from CHUR (εHf), where T is the $^{207}Pb/^{206}Pb$ date obtained for the sample:

$$\varepsilon Hf = \left[\frac{\left(^{176}Hf/^{177}Hf\right)_{sample\ at\ T}}{\left(^{176}Hf/^{177}Hf\right)_{CHUR\ at\ T}} - 1\right] x\ 10^4$$

***Determination of Zr/Hf ratios.*** The zircon and baddeleyite Zr/Hf ratios were acquired after Lu/Hf ratio determination using the leftovers of the 5-10 % aliquots of the U-Pb matrix cuts. In detail, the $^{90}Zr$, $^{91}Zr$, $^{177}Hf$ and $^{178}Hf$ signal intensities were measured on the iCAP™ RQ-ICPMS at the Centre for Star and Planet Formation, Copenhagen. The sample solutions (0.5 M $HNO_3$-0.01 M HF) were aspirated into the plasma source via an Apex HF desolvating nebuliser, and the typical $^{178}Hf$ and $^{90}Zr$ signal intensities were 7000 cps and 300,000 cps, respectively. Sample measurements were bracketed by analyses of the baseline and two Zr/Hf reference solutions in a sequence of baseline – ref1 – ref2 – baseline – sample – sample –sample – sample – sample – baseline – ref1 – ref2 – baseline. The Zr/Hf reference solutions were gravimetrically prepared at the Centre for Star and Planet Formation from two pure element Alfa Aesar™ Specpure™ solutions, with Zr/Hf ratios of 40.7 (ref1) and 50.3 (ref2) and known to a precision of 1.4 %. The data were reduced offline in Microsoft® Excel®. First, the baseline was subtracted to obtain blank-corrected isotope signal intensities. Then, Zr/Hf ratios (not bias-corrected) were calculated from the blank-corrected $^{90}Zr$ and $^{178}Hf$ signal intensities and natural isotope abundance ratios. Finally, instrumental mass bias-corrected Zr/Hf ratios were determined by normalisation to a factor that relates the bias-uncorrected and the true Zr/Hf ratios of the two reference solutions. The reported precisions on the zircon and baddeleyite Zr/Hf ratios were calculated by propagating all sources of uncertainty, which includes the uncertainties associated with the Zr/Hf ratios in the reference solutions, the calculated factor relating the un-bias-corrected and the true Zr/Hf ratios, and the analytical dispersion of the measured signal intensities (20 cycles of measurement) for the specific sample.

We measured the Zr/Hf ratios for aliquots of the Mud Tank zircon (MTZ) and 91500 zircon reference materials alongside the unknown samples to document the reproducibility of the method. In addition to aliquots of unprocessed zircon solutions, we measured the Zr/Hf ratio of three aliquots of MTZ that were processed through the U-Pb chemistry with the aim of assessing the level of Zr/Hf fractionation on the column. The results obtained for MTZ and 91500, respectively, are identical within uncertainty and listed in Table S-2. We note that the Zr/Hf ratios of these two zircon reference materials have, to our knowledge, not been determined to high precision previously, and the results we obtained can therefore not be used as an independent measure of the accuracy of the method.

**Table S-2** The Zr/Hf results for zircon reference materials.

| | Zr [ng] | Zr/Hf | 2SE [%] |
|---|---|---|---|
| *Aliquots of un-processed solution* | | | |
| 91500 | | 84.3 | 3.72 |
| 91500 | | 83.4 | 3.90 |
| 91500 | | 80.1 | 3.10 |
| 91500 | | 85.4 | 3.99 |
| MTZ | | 46.9 | 3.40 |
| *Aliquots after the U-Pb chemistry* | | | |
| MTZ | 25 | 45.9 | 3.06 |
| MTZ | 100 | 45.5 | 2.81 |
| MTZ | 300 | 45.3 | 3.06 |

***Uranium-lead isotope measurements.*** The methods for U-Pb isotope measurements by thermal ionisation mass spectrometry (TIMS) have been described in detail in previous publications (Bouvier *et al.*, 2018; Costa *et al.*, 2020). In summary, the U-Pb cuts were analysed on a Triton Thermo-Fisher™ TIMS at the Centre for Star and Planet Formation, Copenhagen. The U and Pb isotopes were measured using the axial secondary electron multiplier by MassCom™, and the U-Pb isotope data were reduced offline in Microsoft® Excel®. The Pb isotope ratios were corrected for instrumental mass bias using the $^{202}Pb/^{205}Pb$ ratio in the EARTHTIME tracer and a linear mass-dependent fractionation law. Common Pb was assumed to be blank and subtracted using the isotope composition determined previously for the Pb blank in our laboratory with an assigned uncertainty of 1 % on the Pb isotope ratios propagated into the final age uncertainties. The U isotope ratios were corrected for instrumental mass bias using the $^{233}U/^{235}U$ ratio of the EARTHTIME tracer, and a correction for the isobaric interference of $^{233}U^{16}O^{18}O$ on the $^{235}U^{16}O^{2}$ peak at mass 267 was performed using a $^{18}O/^{16}O$ ratio of 0.00205.

The sample concentrations of Pb, U and Th were calculated from the blank- and tracer-subtracted analyte abundances and using the zircon and baddeleyite crystal masses inferred from the measured total Zr abundances (assuming Zr mass fractions of 0.43 and 0.74 for zircon and baddeleyite, respectively). The abundance of Th was estimated from the absolute abundance of radiogenic $^{208}Pb$, a $^{232}Th$ decay constant of $4.94752 \times 10^{-11}$ (Steiger and Jäger, 1977), and the calculated $^{207}Pb/^{235}U$ age of the sample.

## Sample Morphologies, Sizes and Isotope Results

In general, the zircon grains analysed in this study are characterised by a cloudy, granular, and often brownish appearances indicative of metamictisation or partial re-crystallisation (Figs. S-1 to S-3). For some grains, the SEM BSE images reveal a neoblastic tendency, likely indicative of impact metamorphism (*e.g.*, NS5b1-b3 and NS5b14 in Fig. S-2). Most grains are anhedral to subhedral, with just a few grains exhibiting clear remnants of crystal facets such as the baddeleyites in Fig. S-1, and the zircons NS5b14, NS5b8, NS5b13. Some grains are intergrown with other phases, possibly pyroxene and Fe-oxides (*e.g.*, NS5b3, NS5b14). The zircon NS5b6 is subhedral to euhedral with an elongated shape, a morphology that is somewhat closer to that typically observed for magmatic zircon compared to other zircons from NWA 7533.

The masses of the grains range between 8 and 2200 ng (calculated from the measured Zr concentrations in the matrix cut from the U-Pb chemistry), with most grains having masses between 40 and 300 ng (corresponding to 20-130 ng Zr in the case of zircon). The U concentrations calculated using the estimated grain mass typically range between 40 and 80 ppm, similar to the concentrations in NWA 7533 zircon and baddeleyite reported in Costa *et al.* (2020) and as illustrated in Figure S-5c. The Th concentrations of the samples were calculated from radiogenic $^{208}Pb$ with respect to the calculated $^{207}Pb/^{235}U$ date, and the Th/U ratios of the zircons range from 0.3 to 1.3 (Table S-3). We note that the Th contents calculated from radiogenic Pb are crude estimates given the typically discordant U-Pb ages of the analysed samples indicating Pb loss. Nonetheless, the range of Th/U calculated for the samples is overlapping with that of the concordant, old population of zircon reported in Costa *et al.* (2020) with Th/U ratios ranging from 0.4 to 1.5. As such, we believe that the reported Th/U ratios are good approximations of the true ratios. We note that the four baddeleyite samples have Th/U ratios of <0.05 as well as $^{176}Lu/^{177}Hf$ ratios <0.00005 (Table S-3, Fig. S-8b,c). These ratios are at least one order of magnitude lower than in the zircons, reflecting a lower compatibility of Lu and Th in the baddeleyites.

Due to the small grain sizes, the amount of radiogenic Pb is low with typical radiogenic Pb to common Pb ratios ($Pb_{rad}/Pb_c$) between 1 and 15 (Table S-3). This range of $Pb_{rad}/Pb_c$ is similar to that of zircons from Costa *et al.* (2020), which have similar sizes to the grains analysed here (Fig. S-5a,b). Compared to the grain population reported in Costa *et al.* (2020), the samples of this study are, in general, characterised by a higher degree of U-Pb age discordance (Fig. S-5). We note that the higher discordance cannot be attributed to a difference in the typical grain sizes, $Pb_{rad}/Pb_c$ ratios, and U concentrations of the grains.

The stable Zr isotope compositions of the studied samples typically do not exhibit a correlation with the sample sizes (Fig. S-6). This is not surprising given the typically fractured nature of the grains. In other words, the measured sizes of the separated grains do not necessarily reflect the original sizes of the grains. However, in the case of the zircons from clast C28, the smaller grains exhibit heavier Zr isotope compositions (Table S-3). This is consistent with the idea that smaller zircons must have formed later than larger zircons (*i.e.* they had less time to grow) and, therefore, record a more evolved (heavy) isotope composition.

## The Effect of Sample Impurity on Element Ratios

The element ratios measured for zircon can be affected by zircon impurities such as apatite inclusions or attached phases (*e.g.*, pyroxene or Fe-oxide). While such impurities are not expected to affect the Zr isotope compositions, they can potentially alter the element ratios of the sample. This should lead to a decoupling of $\delta^{94}$Zr from the affected elemental ratio. In Figure S-8, we assess the level of decoupling of $\delta^{94}$Zr from the Zr/Hf, Th/U and Lu/Hf elemental ratios due to sample impurity indicated by higher common Pb ($Pb_c$) and/or Th contents (we note that a high Th content is not a diagnostic of an impurity, rather, it is a reasonable indication of impurities such as apatite). We find that the Zr/Hf ratio is apparently not affected by the presence of sample impurities, since the samples with high $Pb_c$ and Th do not deviate from the trend defined by the other samples (Fig. S-8a). Likewise, the Lu/Hf ratio is not significantly affected by sample impurities, except for the zircon NS4b6 with a relative high Lu/Hf ratio (coupled with a high Th/U ratio), likely indicating apatite inclusions (Fig. S-8b). On the contrary, the Th/U ratios of samples with high $Pb_c$ (>4 pg) and/or Th (>80 ppm) appear to be highly decoupled from the $\delta^{94}$Zr-Th/U trend defined by the other samples. In detail, the samples with high $Pb_c$ and Th extend towards higher Th/U ratios, indicating that the sample compositions are affected by a high-Th/U impurity (Fig. S-8c). Given that the Th/U ratios in these samples do not correlate with $\delta^{94}$Zr, the presence of a high-Th/U impurity does not affect the $\delta^{94}$Zr composition. As mentioned in the previous section, we emphasise that the deviation of the four baddeleyites from the zircons with regards to Lu/Hf and Th/U likely reflects a lower compatibility of Lu and Th in this mineral. In conclusion, we find that some samples exhibit altered Lu/Hf and Th/U ratios due to impurities, but we observe no discernible effect on the stable Zr isotope compositions nor the Zr/Hf ratios of the investigated samples.

## Sample NS5b6 – A Metamorphic Grain?

The elongated zircon NS5b6 has a radiogenic Hf isotope composition relative to the zircons with similar Lu/Hf ratios indicating the incorporation of radiogenic Hf after initial crystallisation (Fig. S-9). Further, NS5b6 exhibits an anomalously low Th/U ratio (0.05) similar to that observed in metamorphic zircons (Rubatto, 2002) and high U (~1200 ppm) relative to the other NWA 7533 zircons, indicating a unique origin or history for this grain. Together with the unique near-euhedral morphology (Fig. S-3), and the almost completely reset U-Pb isotope systematics of the grain (Fig. S-4), we, therefore, suspect that NS5b6 represents a metamorphic zircon. We stress that the conclusions drawn in this study are not dependent on the isotope composition of NS5b6.

## Rayleigh Fractionation Modelling

Rayleigh fractionation is based on the principle of negligible isotopic exchange between the formed solid and the melt, and this could be due to either slow diffusion in the solid or segregation of the solid from the melt. Since Zr diffusion in zircon is very slow (Cherniak *et al.*, 1997), Rayleigh fractionation is a reasonable model to describe the stable Zr isotope fractionation occurring during zircon crystallisation. Assuming that zircon is the only phase incorporating Zr, the Zr isotope composition of the melt and the instantaneous zircon crystallising from the melt can be expressed as:

$$\delta^{94}Zr_{\mathrm{melt}} = \delta^{94}Zr_0 + \Delta^{94}Zr_{\mathrm{zircon-melt}} \ln f_{Zr},$$

and

$$\delta^{94}Zr_{\text{zircon}} = \delta^{94}Zr_0 + \Delta^{94}Zr_{\text{zircon-melt}}(1 + \ln f_{Zr}),$$

where $\delta^{94}Zr_{melt}$, $\delta^{94}Zr_0$ and $\delta^{94}Zr_{zircon}$ are the Zr isotope compositions in the residual melt, the initial melt and the instantaneous zircon crystallising from the melt, $f_{Zr}$ is the fraction of Zr remaining in the melt, and $\Delta^{94}Zr_{\text{zircon-melt}}$ is the fractionation factor between zircon and melt (*i.e.* a measure of the magnitude of mass dependent Zr isotope fractionation occurring as Zr is exchanged between the two). $\Delta^{94}Zr_{\text{zircon-melt}}$ can be expressed as:

$$\Delta^{94}Zr_{\text{solid-melt}} = 1000\ln(\alpha_{solid-melt}),$$

where $\alpha_{\text{solid-melt}}$ is:

$$\alpha_{solid-melt} = \left(\frac{^{94}Zr}{^{90}Zr}\right)_{solid} \Big/ \left(\frac{^{94}Zr}{^{90}Zr}\right)_{melt}$$

Like $\delta^{94}Zr$, the fractionation of Zr/Hf induced by zircon crystallisation can also be described by Rayleigh fractionation:

$$(Zr/Hf)_{\text{melt}} = (Zr/Hf)_0 \, f_{\text{Zr}}^{1 - 1/(K_d^{Zr}/K_d^{Hf})}$$
$$(Zr/Hf)_{\text{zircon}} = K_d^{Zr}/K_d^{Hf}(Zr/Hf)_0 \, f_{\text{Zr}}^{1 - 1/(K_d^{Zr}/K_d^{Hf})}$$

Where the subscript "0" denotes the initial composition, and $K_d^{Zr}/K_d^{Hf}$ is the ratio of the partition coefficients for Zr and Hf between zircon and melt. This partition coefficient ratio has been proposed to follow a temperature dependence for zircon under thermodynamic equilibrium conditions described as (Aranovich and Bortnikov, 2018):

$$K_d^{Zr}/K_d^{Hf} = \frac{C_{Zr}^{solid}}{C_{Zr}^{melt}} \Big/ \frac{C_{Hf}^{solid}}{C_{Hf}^{melt}} = e^{(1531/T - 0.883)},$$

where $C_j^i$ is the concentration of element j in phase i, and T is the temperature in Kelvin. We note that the corresponding relationship for baddeleyite is unknown. Thus, the $K_d^{Zr}/K_d^{Hf}$ that best describes the evolution of the melt may deviate from the value predicted from the above equation if zircon and baddeleyite are co-crystallising.

The equilibrium Rayleigh fractionation curves are generated using the temperature-dependent zircon-melt equilibrium fractionation factor, and the temperature-dependent zircon-melt Zr-Hf partition coefficient ($Kd^{Zr}/Kd^{Hf}$) derived by Aranovich and Bortnikov (2018). The temperature-dependent zircon-melt equilibrium fractionation factor is calculated as:

$$\Delta^{94}\text{Zr}_{\text{zircon-melt}} = \frac{(A1_{zrn} - A1_{melt}) * 10^6}{T^2} + \frac{(A2_{zrn} - A2_{melt}) * 10^{12}}{T^4} - \frac{(A3_{zrn} - A3_{melt}) * 10^{18}}{T^6}$$

Where T is the temperature in Kelvin, and the A1, A2, and A3 coefficients for zircon and Ca-catapleeite (as a proxy for silicate melt) can be found in Table 1 in Chen *et al.* (2020).

We emphasise that the predicted equilibrium Zr isotope fractionation between baddeleyite and melt is of similar magnitude to that calculated for zircon and can, thus, be approximated by the zircon isotope fractionation curves (Chen *et al.*, 2020).

## Equilibrium *versus* Kinetic Isotope Fractionation

For temperatures of 700 ºC and 1000 ºC, the equilibrium fractionation factors between zircon and melt, $\Delta^{94}Zr_{zircon-melt}$, are -0.081 ‰ and -0.048 ‰, corresponding to α values of 0.99992 and 0.99995, respectively (refer to the previous section for calculation details). This means that, assuming a martian mantle initial $\delta^{94}Zr_{IPGP\text{-}Zr}$ melt composition (0.062 ± 0.043 ‰, Jensen *et al.*, 2025a), the lightest isotope composition that can be produced by fractional crystallisation of zircon and baddeleyite is $\delta^{94}Zr_{IPGP\text{-}Zr}$ = -0.019 ‰ under purely equilibrium conditions at 700 ºC. We stress that the zircons with the highest Zr/Hf ratios (indicating relatively early crystallisation) exhibit $\delta^{94}Zr_{IPGP\text{-}Zr}$ of -0.139 ± 0.016 ‰ (NS4b8) and -0.281 ± 0.011 ‰ (NS5b5, Table S-3), values that would require significantly lower initial $\delta^{94}Zr_{IPGP\text{-}Zr}$ melt compositions to be explained by equilibrium fractionation alone. As an example, for a temperature of 850 ºC and an initial $\delta^{94}Zr_{IPGP\text{-}Zr}$ melt composition of -0.075 ‰ (and Zr/Hf = 39), the zircon NS4b8 with $\delta^{94}Zr_{IPGP\text{-}Zr}$ = -0.139 ± 0.016 ‰ can be explained by equilibrium-only Zr isotope fractionation (Fig. S-12, α = 0.99994, $Kd^{Zr}/Kd^{Hf}$ = 1.6). This model, however, can only explain a small fraction of the all the analysed grains. In detail, the slope of the Rayleigh fractionation curve in Figure S-12 is too small to fit the zircon and baddeleyite grains with lower Zr/Hf ratios.

We stress that the slope of the Rayleigh fractionation curves in a plot of $\delta^{94}Zr_{IPGP\text{-}Zr}$ versus Zr/Hf is dependent not only on α, but also on the mineral-melt Zr-Hf partition coefficient ($Kd^{Zr}/Kd^{Hf}$). For the equilibrium curves in Figure 3 and S-12, we used the temperature-dependent $Kd^{Zr}/Kd^{Hf}$ expression of Aranovich and Bortnikov (2018) that predicts zircon-melt $Kd^{Zr}/Kd^{Hf}$ values of 2.0, 1.6, and 1.4 for 700 ºC, 850 ºC and 1000 ºC, respectively. However, it is unknown if this $Kd^{Zr}/Kd^{Hf}$ expression is valid for all melt compositions, and for the co-crystallisation of baddeleyite with zircon. Therefore, we further model the Zr isotope evolution of the system using arbitrary values for $Kd^{Zr}/Kd^{Hf}$ in combination with equilibrium stable Zr isotope fractionation. We find that for an arbitrary set of parameters ($Kd^{Zr}/Kd^{Hf}$ = 1.2, initial $\delta^{94}Zr_{IPGP\text{-}Zr}$ = -0.07 ‰, initial Zr/Hf = 51) and equilibrium Zr isotope fractionation at 800 ºC (α = 0.99993), the Rayleigh fractionation curve fits the trend defined by 21 out of 26 grains (Fig. S-13). This could indicate that this fraction of the zircon/baddeleyite grains record equilibrium-only or near-equilibrium stable Zr isotope fractionation. However, we emphasise that this model is based on fitting several free parameters, namely the initial melt $\delta^{94}Zr_{IPGP\text{-}Zr}$ and Zr/Hf compositions and $Kd^{Zr}/Kd^{Hf}$. Given that arbitrary values were chosen for all these parameters, and the fact that this model cannot explain the five zircon and baddeleyite grains with most extreme Zr isotope compositions, we argue that a combination of equilibrium and kinetic isotope fractionation is required to explain the stable Zr isotope compositions of the investigated grains. In fact, the values set for the initial melt composition in the model in Figure S-13 are completely unconstrained and, arguably, unrealistic given the significantly heavier bulk stable Zr isotope compositions observed for NWA 7533 clasts (Jensen *et al.*, 2025a, plotted in Fig. 4 and Fig. S-11). Finally, we suggest that future work is aimed at further constraining the temperature-dependent (equilibrium) Zr-Hf partition coefficient for zircon and baddeleyite and the dependence of this parameter on the melt composition. This will aid future evaluations of the relative contributions of equilibrium and kinetic stable Zr isotope fractionation.

## Clast C28 Zircons

As described in the main text, the two larger zircons from clast C28 (NS6b13 and NS6b14) have lighter Zr isotope compositions ($\delta^{94}Zr_{IPGP\text{-}Zr}$ ~ -0.250 ‰) relative to the three other zircons from this clast (with $\delta^{94}Zr_{IPGP\text{-}Zr}$ ~ 0 ‰). We find that the stable Zr isotope compositions of the five zircons from clast C28 cannot be explained by a single Rayleigh fractionation model if assuming an initial melt composition akin to the bulk composition of the host clast. However, with the assumption of an initial melt composition similar to the martian mantle ($\delta^{94}Zr_{IPGP\text{-}Zr}$ = 0.062 ± 0.043 ‰, Jensen *et al.*, 2025a), all five zircons can be matched by a Rayleigh fractionation model with α = 0.99955-0.99965 and $Kd^{Zr}/Kd^{Hf}$ = 1.4 (Fig. S-11). If this model is correct, the clast represents a cumulate rock, and its Zr isotope composition should be a mixture of the zircons it entrains. However, the clast plots off the trajectory defined by the five zircons, indicating that the Zr/Hf ratio was decoupled from $\delta^{94}Zr$ during the cumulate formation, or that the model is inaccurate.

It should be mentioned that the three zircons with a heavier Zr isotope composition are very small, with only about 3-7 ng Zr available for the stable Zr isotope analysis resulting in 4-7 V of total Zr signal during the analysis (Table S-4,

available for download from the online version of this article). This amount of Zr is significantly lower than the 25 ng of Zr used in previous low-Zr tests conducted for the Mud Tank Zircon, which yielded accurate results (Jensen *et al.*, 2024). Importantly, the measurements of the Mud Tank Zircon were conducted with 25-30 V of total Zr signal (and typically 44 cycles of measurement with 8.4 s integration time), which is several times higher than the total signal during the analysis of the small C28 zircons. While the blank of the full chromatographic procedure (10-40 pg Zr, Jensen *et al.*, 2024) is too low to have a discernible effect on the sample compositions, the measurements could have been associated with analytical artefacts leading to biased results. However, such analytical artefacts have not been identified, and further tests would be required to confirm the effect for samples with <10 ng Zr. Moreover, the small C28 zircons follow the general $\delta^{94}$Zr-Zr/Hf trend of the NWA 7533 zircon/baddeleyite grains which would not be expected if the $\delta^{94}$Zr results were biased (Fig. 4). Therefore, the most consistent model is that the C28 zircons crystallised from a C28-like initial melt, with the stable Zr isotope composition of this melt being modified by kinetic isotope fractionation. Finally, we note that the investigation of additional zircons from this clast are required to confirm a parental melt with a composition distinct from that of the host clast.

# Supplementary Tables

**Table S-3** Summary of the U-Pb, Lu-Hf, and Zr isotope results for NWA 7533 zircon and baddeleyite. Full results are reported in Table S-4.

| | Mass [ng][a] | Pb*/Pbc | U [ppm][b] | Th/U[b] | Zr/Hf | $^{207}Pb/^{206}Pb$ age [Myr] ± 2SE | Disc. [%][c] | $^{176}Lu/^{177}Hf$ | $^{176}Hf/^{177}Hf$[d] ± 2SE | $\varepsilon Hf_T$[e] | $\delta^{94}Zr_{IPGP\text{-}Zr}$ [‰] ± 2SE | n[f] | scans/n[f] |
|---|---|---|---|---|---|---|---|---|---|---|---|---|---|
| *NWA 7533 baddeleyite* | | | | | | | | | | | | | |
| NS4b1 | 123 | 10.8 | 79 | 0.01 | 35 | 4255.6 ± 0.9 | 0.4 | 0.00002 | 0.279896 ± 16 | -4.0 ± 0.6 | 0.468 ± 0.009 | 3 | 35 |
| NS4b5 | 35 | 2.9 | 23 | 0.05 | 40 | 4444.5 ± 3.1 | 0.1 | 0.00003 | 0.279825 ± 46 | -2.0 ± 1.7 | 0.254 ± 0.009 | 1 | 50 |
| NS5b4 | 209 | 3.2 | 34 | 0.00 | 49 | 4336.4 ± 2.3 | 0.7 | 0.00002 | 0.279859 ± 12 | -3.4 ± 0.6 | -0.093 ± 0.005 | 5 | 43 |
| NS5b16 | 44 | 16.5 | 157 | 0.01 | 29 | 4468.8 ± 1.0 | 0.8 | 0.00005 | 0.279840 ± 30 | -0.9 ± 1.1 | 0.194 ± 0.015 | 1 | 44 |
| *NWA 7533 zircon* | | | | | | | | | | | | | |
| NS4b2 | 336 | 21.0 | 51 | 0.45 | 56 | 4177.0 ± 0.6 | 28.4 | 0.00093 | 0.279922 ± 15 | -7.6 ± 0.7 | -0.118 ± 0.009 | 3 | 50 |
| NS4b3 | 135 | 5.9 | 44 | 0.44 | 55 | 4187.7 ± 1.8 | 28.0 | 0.00089 | 0.279884 ± 29 | -8.6 ± 1.7 | -0.078 ± 0.010 | 1 | 50 |
| NS4b4 | 90 | 3.0 | 57 | 0.36 | 56 | 4197.1 ± 3.3 | 27.8 | 0.00093 | 0.279896 ± 26 | -8.1 ± 1.7 | -0.085 ± 0.011 | 1 | 50 |
| NS4b6 | 35 | 4.1 | 242 | 1.29 | 46 | 2815.5 ± 16.4 | 44.6 | 0.00257 | 0.280180 ± 31 | -33.1 ± 1.7 | 0.002 ± 0.021 | 1 | 33 |
| NS4b7 | 44 | 0.5 | 40 | 0.73 | 52 | 4520.5 ± 11.8 | 5.2 | 0.00113 | 0.279949 ± 32 | 0.8 ± 1.7 | -0.075 ± 0.016 | 1 | 33 |
| NS4b8 | 41 | 0.8 | 39 | 0.53 | 61 | 4449.5 ± 8.9 | 10.3 | 0.00130 | 0.279993 ± 67 | 0.2 ± 2.4 | -0.139 ± 0.016 | 1 | 33 |
| NS5b1 | 234 | 3.8 | 43 | 0.45 | 56 | 4130.8 ± 2.9 | 31.5 | 0.00094 | 0.279929 ± 22 | -8.5 ± 0.8 | -0.087 ± 0.012 | 3 | 41 |
| NS5b2 | 2210 | 53.6 | 46 | 0.48 | 59 | 4278.1 ± 0.2 | 22.0 | 0.00121 | 0.279921 ± 12 | -6.1 ± 0.7 | -0.143 ± 0.008 | 5 | 50 |
| NS5b3 | 1316 | 13.1 | 48 | 0.44 | 57 | 4292.0 ± 1.7 | 20.8 | 0.00101 | 0.279911 ± 13 | -5.5 ± 0.7 | -0.131 ± 0.011 | 5 | 50 |
| NS5b5 | 87 | 3.7 | 38 | 0.74 | 62 | 4479.8 ± 1.9 | 0.7 | 0.00170 | 0.280013 ± 27 | 0.4 ± 1.8 | -0.281 ± 0.011 | 1 | 42 |
| NS5b6 | 185 | 6.5 | 1242 | 0.05 | 33 | 1894.7 ± 10.3 | 24.9 | 0.00071 | 0.281091 ± 14 | -18.1 ± 0.6 | 0.162 ± 0.010 | 3 | 37 |
| NS5b7 | 197 | 2.9 | 42 | 0.45 | 59 | 4255.7 ± 3.2 | 24.6 | 0.00101 | 0.279893 ± 23 | -7.0 ± 0.8 | -0.123 ± 0.015 | 3 | 41 |
| NS5b8 | 41 | 0.3 | 48 | 1.05 | 47 | 4499.8 ± 19.5 | 12.2 | 0.00114 | 0.279854 ± 54 | -3.1 ± 2.0 | -0.034 ± 0.019 | 1 | 44 |
| NS5b13 | 150 | 3.8 | 50 | 0.51 | 58 | 4271.0 ± 2.4 | 23.4 | 0.00133 | 0.279963 ± 30 | -5.1 ± 1.7 | -0.142 ± 0.025 | 3 | 32 |
| NS5b14 | 264 | 2.6 | 49 | 0.43 | 56 | 4268.7 ± 3.5 | 23.9 | 0.00097 | 0.279932 ± 13 | -5.2 ± 0.7 | -0.117 ± 0.010 | 3 | 50 |
| NS5b15 | 169 | 7.7 | 42 | 0.44 | 57 | 4251.9 ± 1.3 | 24.4 | 0.00087 | 0.279895 ± 25 | -6.6 ± 0.9 | -0.080 ± 0.019 | 3 | 36 |
| NS6b16 | 44 | 1.7 | 71 | 0.33 | 56 | 4186.9 ± 6.5 | 31.4 | 0.00105 | 0.279954 ± 85 | -6.6 ± 3.1 | -0.129 ± 0.028 | 1 | 50 |
| *C28 zircon* | | | | | | | | | | | | | |
| NS6b2 | 13 | 0.7 | 112 | 0.95 | 42 | 3518.1 ± 35.4 | 44.9 | | | | 0.006 ± 0.052 | 1 | 35 |
| NS6b4 | 19 | 1.1 | 71 | 1.13 | 45 | 3571.9 ± 24.1 | 43.0 | | | | -0.031 ± 0.031 | 1 | 35 |
| NS6b13 | 88 | 11.6 | 74 | 0.55 | 51 | 4250.5 ± 1.2 | 23.3 | 0.00177 | 0.279927 ± 19 | -8.2 ± 1.7 | -0.235 ± 0.018 | 1 | 43 |
| NS6b14 | 214 | 16.8 | 93 | 0.60 | 51 | 4098.1 ± 0.9 | 31.6 | 0.00199 | 0.280030 ± 26 | -8.6 ± 1.0 | -0.250 ± 0.014 | 3 | 50 |
| NS6b15 | 8 | 0.3 | 131 | 0.30 | 44 | 4100.8 ± 31.9 | 40.8 | | | | -0.026 ± 0.063 | 1 | 20 |

[a]The crystal masses are calculated from the measured Zr content and a Zr mass fraction of 0.43 and 0.73 in zircon and baddeleyite, respectively.
[b]The amount of Th is calculated from the amount of radiogenic $^{208}Pb$ with respect to the $^{207}Pb/^{235}U$ age, and the U and Th concentrations are calculated using the estimated crystal mass.
[c]The U-Pb age discordance is calculated from the $^{206}Pb/^{238}U$ and $^{207}Pb/^{206}Pb$ ages according to: $(1-(t^{206}Pb/^{238}U)/(t^{207}Pb/^{206}Pb))*100\%$.
[d]Uncertainties on the Hf isotope ratios reflect the 2SE internal precision in the last decimal places.
[e]εHf values are calculated relative to CHUR using the parameters from Bouvier *et al.* (2008) and the $^{207}Pb/^{206}Pb$ ages.
[f]n and scans/n reflect the number of Zr measurements and the number of scans (8.4 s integration time) per measurement.

**Table S-4** Full U-Pb, Lu-Hf, and Zr isotope results for NWA 7533 zircon and baddeleyite.

Table S-4 (.xlsx) is available for download from the online version of this article at https://doi.org/10.7185/geochemlet.2604.

## Supplementary Figures

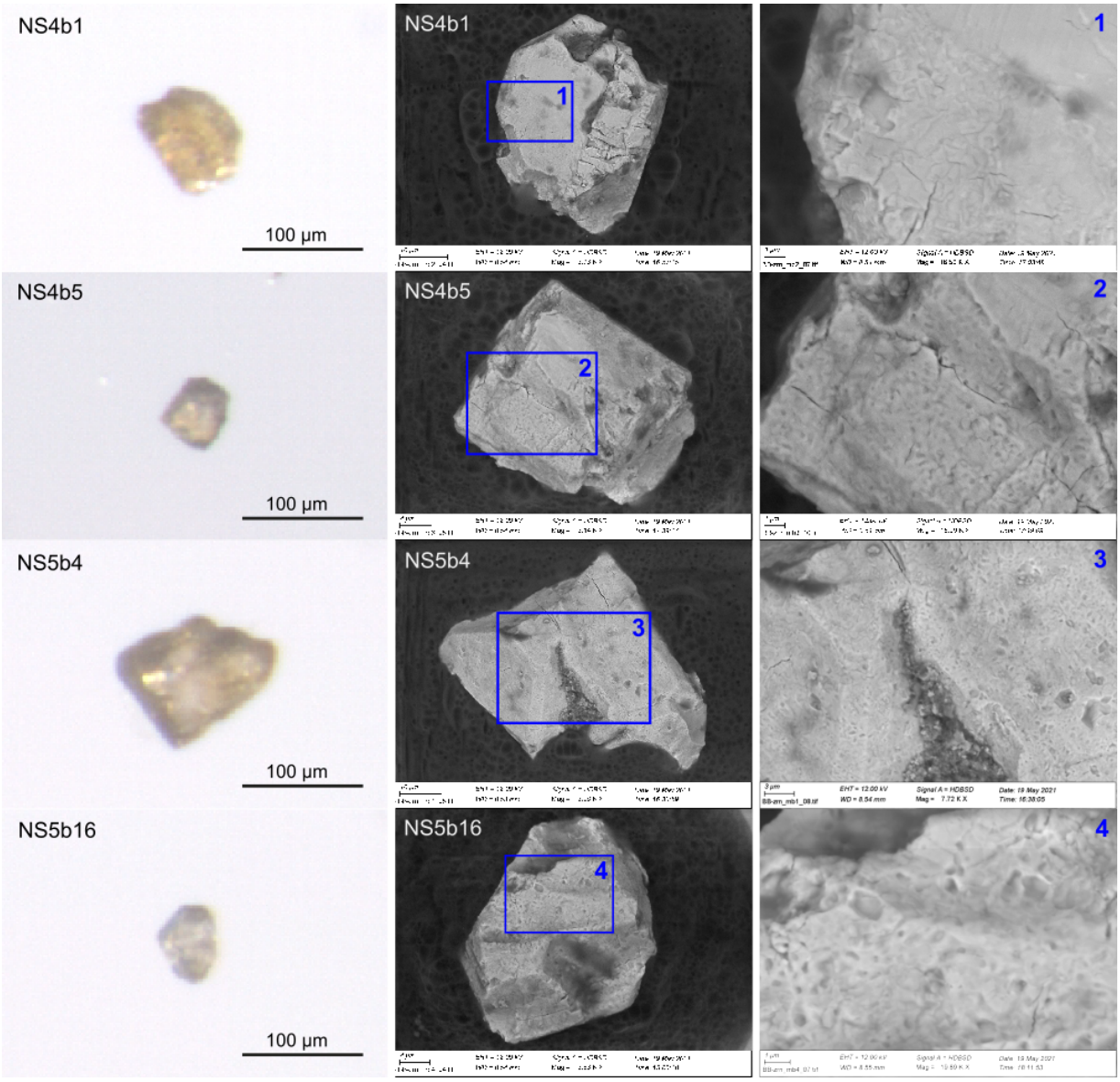


**Figure S-1** Optical light photomicrographs and BSE images of the four baddeleyite grains analysed in this study.

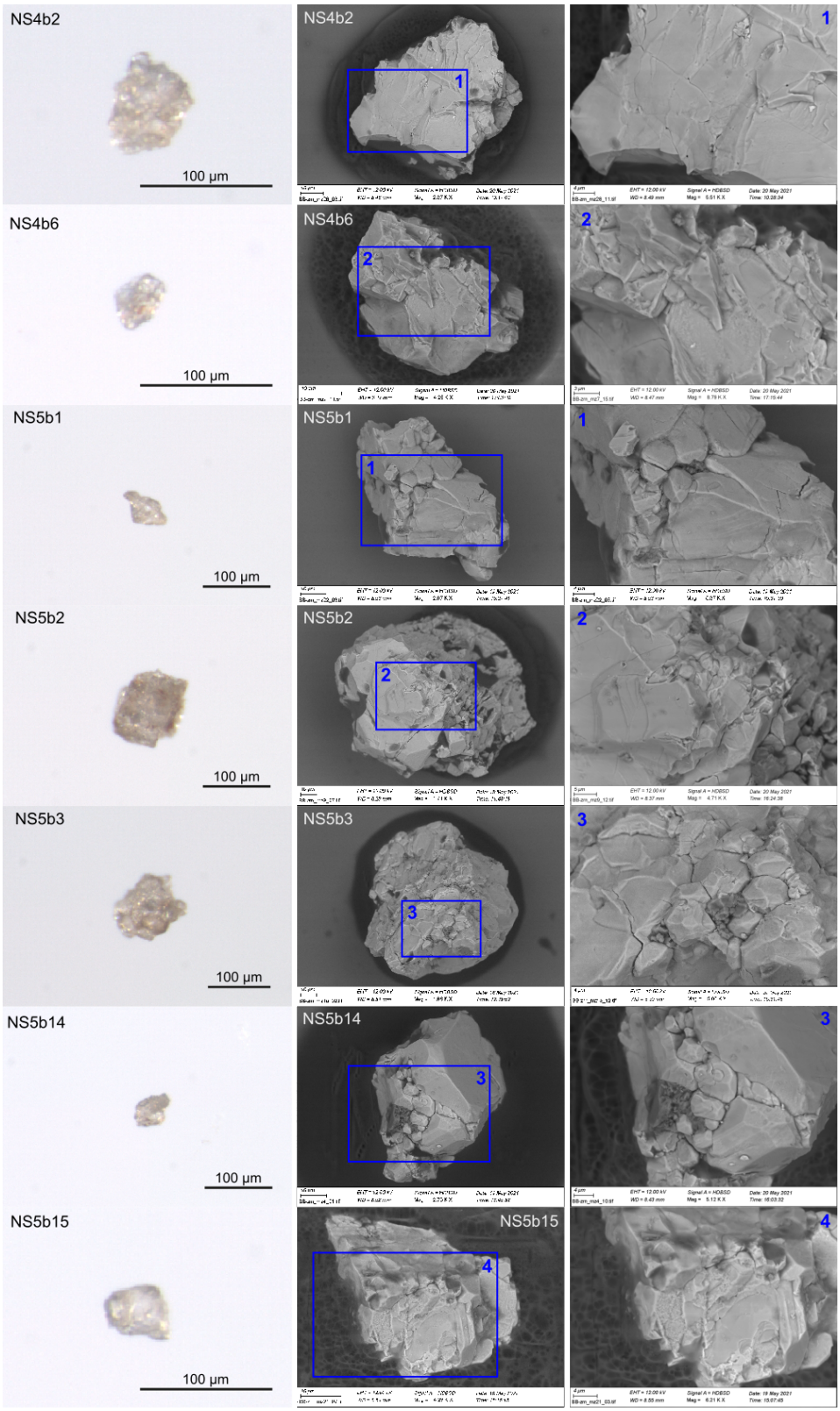


**Figure S-2** Optical light photomicrographs and BSE images of granular zircons. Note the neoblastic tendency of the grains NS5b1-b3 and NS5b14.

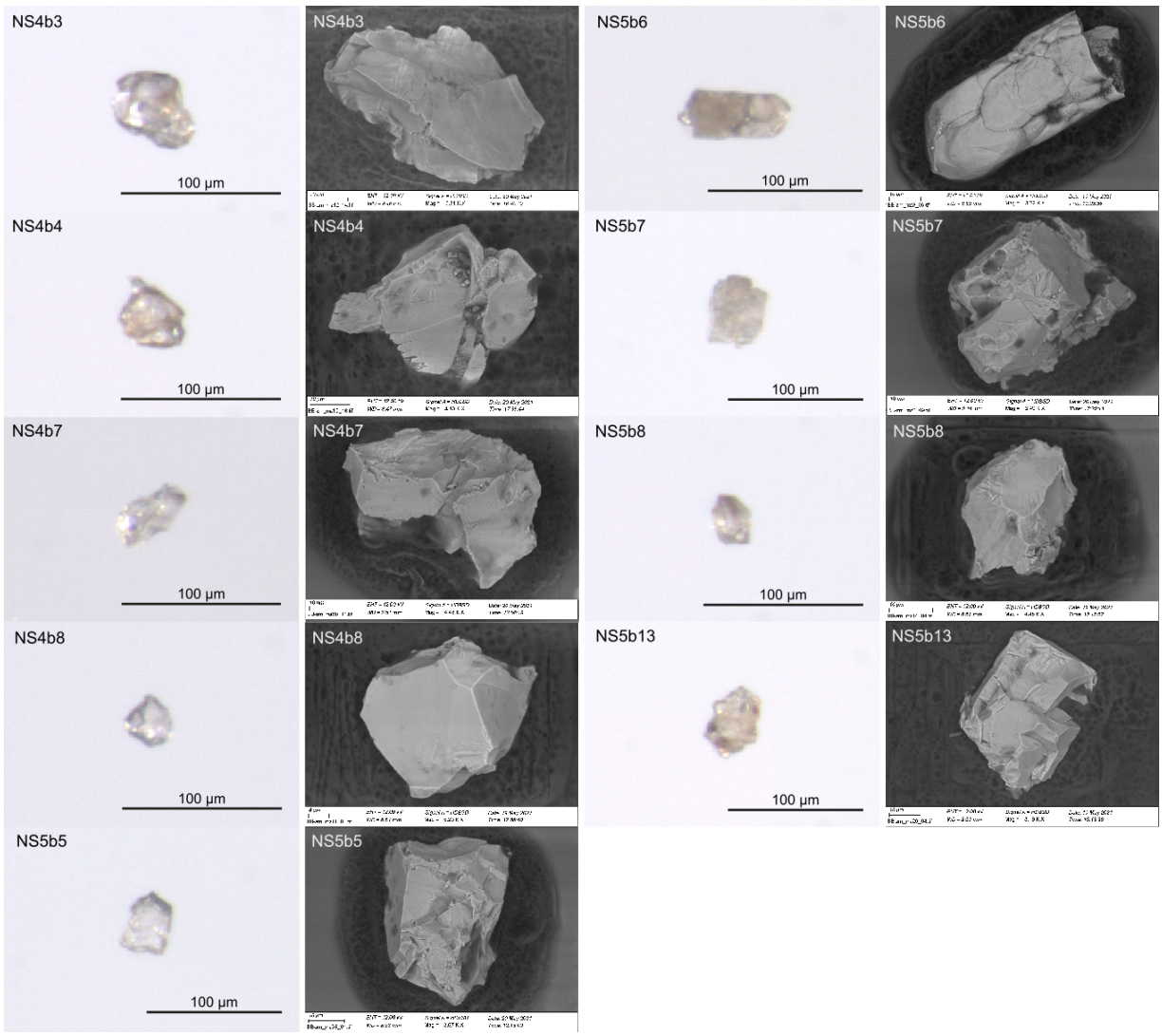


**Figure S-3** Optical light photomicrographs and BSE images of other zircons. Note the nearly euhedral morphology of the grain NS5b6.

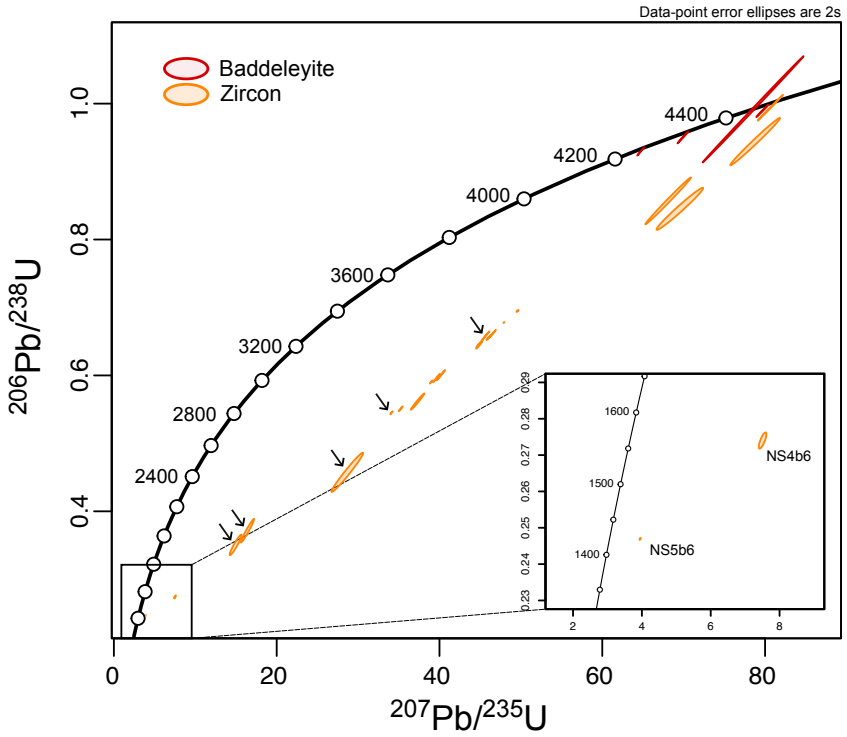


**Figure S-4** Wetherill diagram illustrating the U-Pb isotope compositions of the investigated NWA 7533 zircon and baddeleyite grains. Five grains yield concordant U-Pb ages. The clast C28 zircon U-Pb data are from Jensen *et al.* (2025b) and indicated with arrows. The inset shows a close-up of the grains NS4b6 and NS5b6 which exhibit almost completely reset U-Pb isotope systematics.

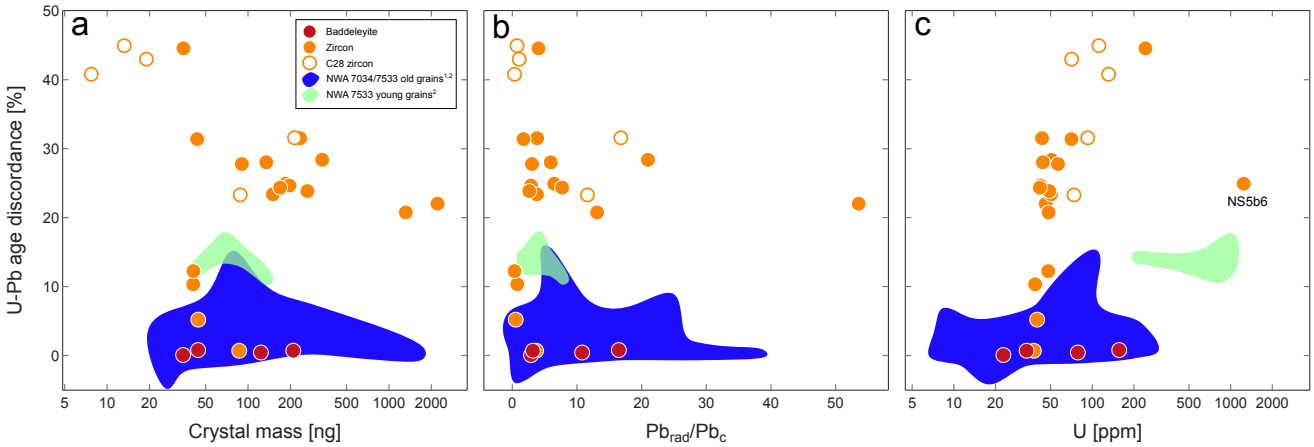


**Figure S-5** A comparison between the NWA 7533 grains of this study and the NWA 7034/7533 sample data reported in 1: Bouvier *et al.* (2018) and 2: Costa *et al.* (2020). The literature data is illustrated with coloured fields and divided into two groups, respectively, the old and the young grain population. The coloured area corresponding to the young population reflects five out of eight young grains (the last three grains have U-Pb age discordances outside of the plotted range) reported in Costa *et al.* (2020).

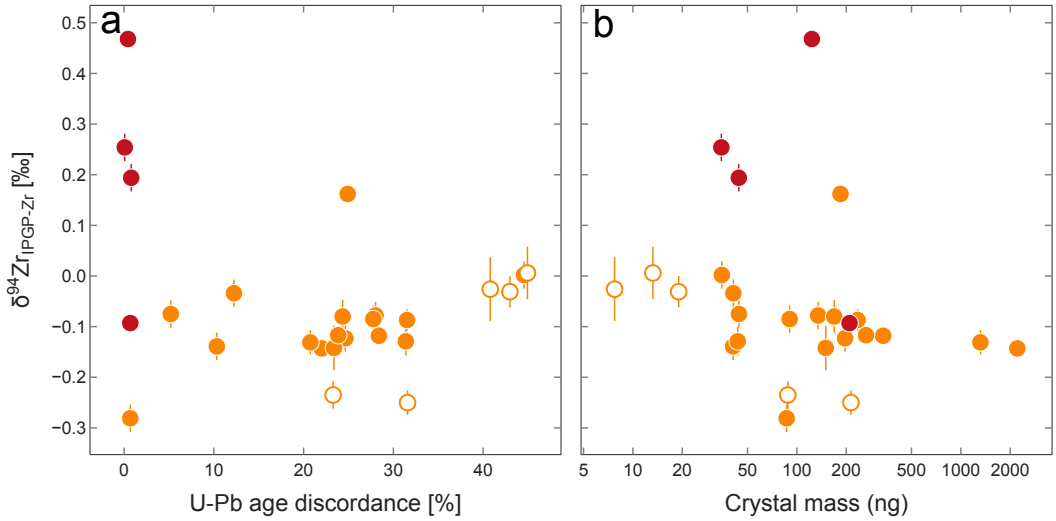


**Figure S-6** The stable Zr isotope compositions of NWA 7533 mineral grains plotted against U-Pb age discordance (a) and crystal mass (b). The plotted Zr isotope uncertainties reflect the 2SD internal precision or external reproducibility, whichever is the largest. Note the logarithmic x-axis in panel (b).

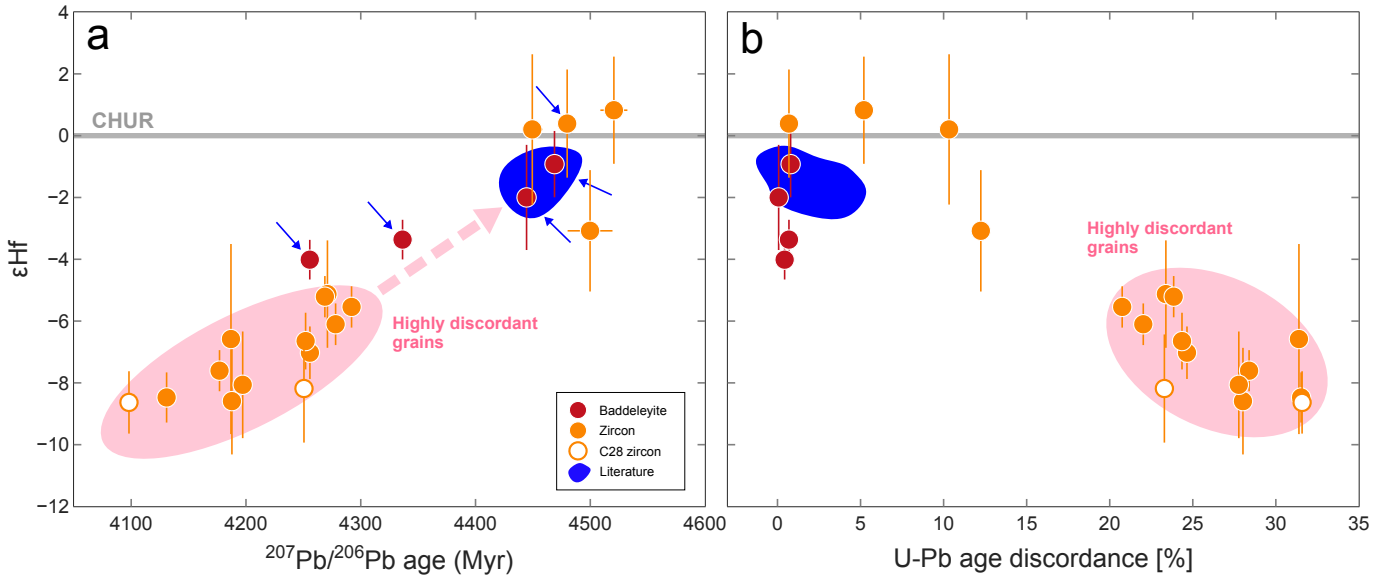


**Figure S-7** Epsilon-Hf (εHf) versus time (a) and U-Pb age discordance (b). The εHf value was calculated for the $^{207}Pb/^{206}Pb$ date and, in the case of the concordant samples, reflects the initial isotope composition. The highly discordant samples define an εHf-time array that extrapolates back to the concordant (<5 % discordant) old NWA 7034/7533 zircon population from the literature, indicated by the blue area (panel a). The literature data in blue are from Bouvier *et al.* (2018) and Costa *et al.* (2020), and the data for C28 zircon are from Jensen *et al.* (2025b). The blue arrows indicate the NWA 7533 samples of this study with a discordance <5 %. Panel b illustrates the level of discordance in the samples. The CHondritic Uniform Reservoir is indicated with a grey line at εHf = 0 and is based on Bouvier *et al.* (2008).

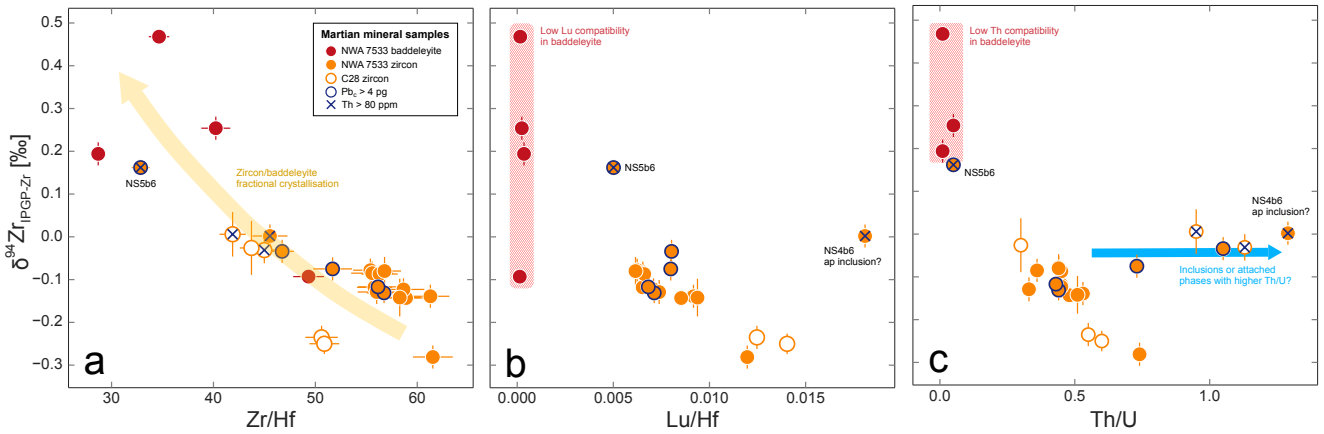


**Figure S-8** The stable Zr isotope composition versus the Zr/Hf (a), Lu/Hf (b), and Th/U (c) ratios in the NWA 7533 samples. Samples with a common Pb content greater than 4 pg are indicated with a blue marker border, and samples with a calculated Th concentration higher than 80 ppm are indicated with a blue cross. A high common Pb content or Th concentration may indicate the presence of inclusions or attached phases in the dissolved sample (*i.e.* sample impurity). Panel (a) shows that the correlation between $\delta^{94}$Zr and Zr/Hf is unaffected by potential sample impurity, possibly due to the low amounts of Zr and Hf in the impurity phase. On the other hand, the Th/U ratios are apparently highly affected by sample impurities, identified by the extension of a group of samples towards higher Th/U (panel c). The Lu/Hf ratios are less affected, with just one sample (NS4b6) clearly deviating from the main trend towards a higher Lu/Hf ratio, likely indicating the presence of apatite (ap) inclusions.

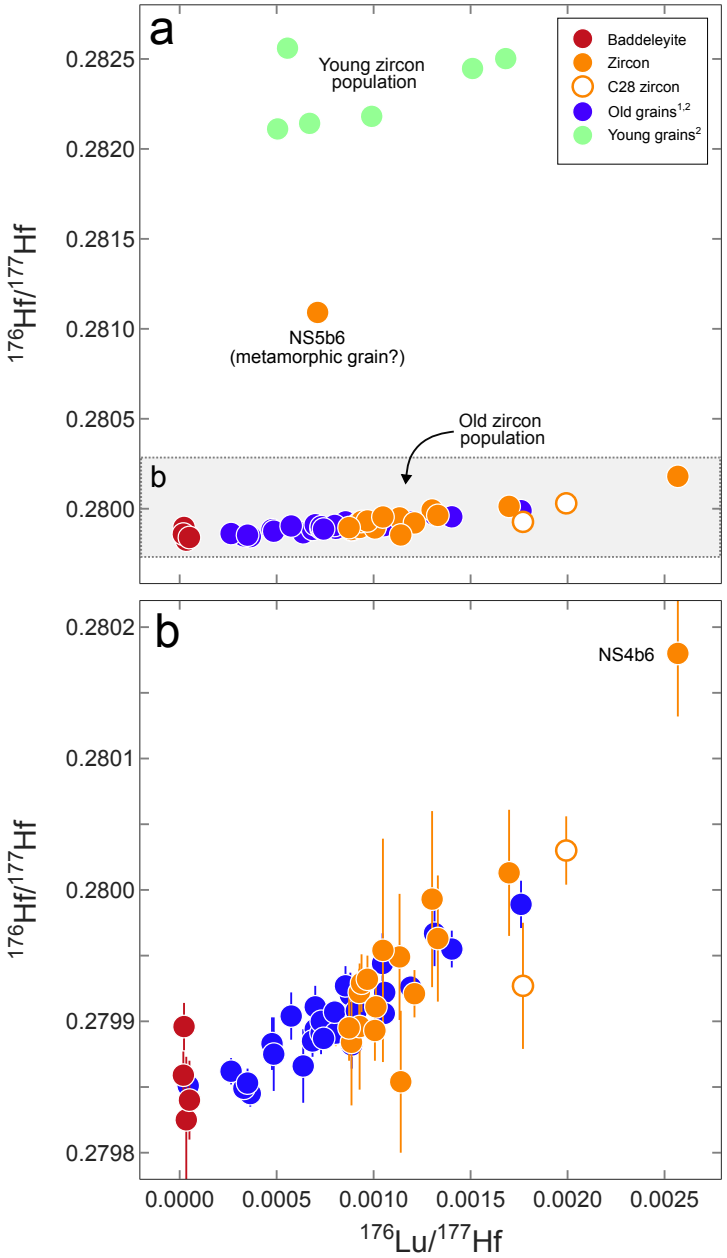


**Figure S-9** The Lu-Hf isotope compositions of NWA 7533 grains of this study and the NWA 7034/7533 zircon and baddeleyite data reported in 1: Bouvier *et al.* (2018) and 2: Costa *et al.* (2020). The literature data is divided into two groups, respectively, the old and the young grain population. The grey shaded field in panel a indicates the compositional range visualised in panel b. Panel b shows that the samples analysed in this study overlap the Lu-Hf isotopic trend defined by the concordant NWA 7034/7533 grains from the literature. The error bars on the data from this study reflect the 2SE internal precision or the external reproducibility, whichever is the largest. The error bars on the literature data reflect the reported 2SE uncertainties.

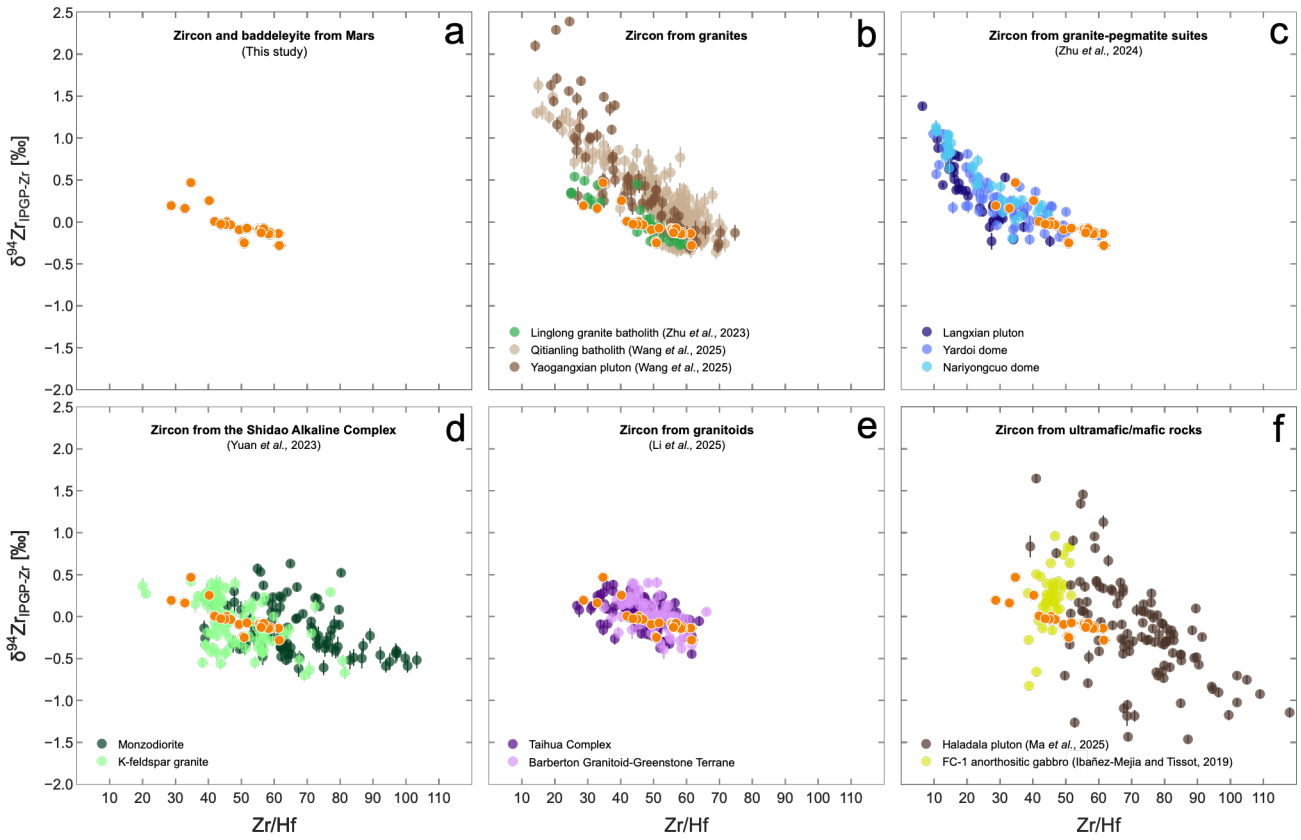


**Figure S-10** The stable Zr isotope and Zr/Hf compositions of the NWA 7533 zircon and baddeleyite from this study plotted together with literature terrestrial zircon data. Note that the terrestrial zircon data were obtained by LA-MC-ICPMS and reflect both inter- and intra-grain variability. The error bars on the literature data reflect 2SE, and the error bars on the data from this study reflect the 2SD internal precision or external reproducibility, whichever is the largest.

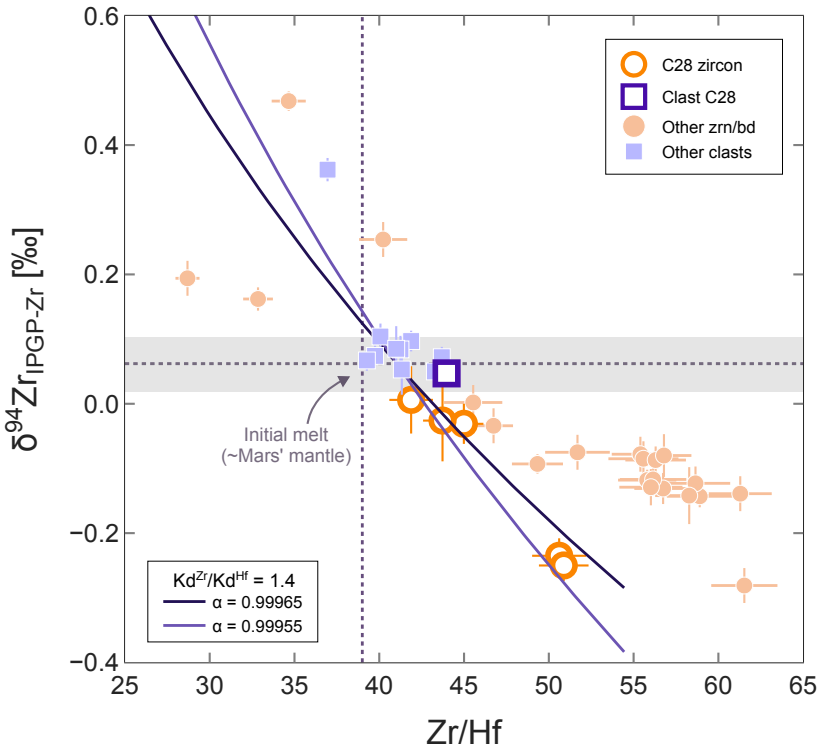


**Figure S-11** Rayleigh fractionation curves assuming an initial Zr isotope composition akin the martian mantle (Jensen *et al.*, 2025a) and an initial Zr/Hf ratio of 39. These model curves can reproduce the isotope composition of all C28 zircons, but the model cannot explain the isotope composition of the host clast.

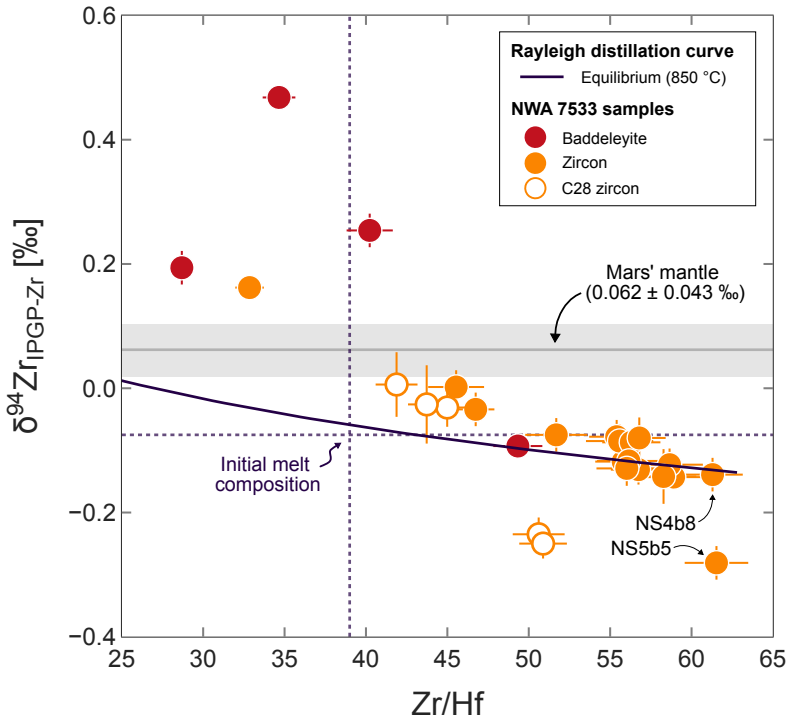


**Figure S-12** Rayleigh fractionation curve reflecting equilibrium fractionation at 850 ºC ($\alpha$ = 0.99994, $Kd^{Zr}/Kd^{Hf}$ = 1.6). The dotted lines illustrate the initial melt composition used for the isotope fractionation model. The composition of the zircon NS4b8 can be explained by equilibrium-only isotope fractionation at 850 ºC if setting the initial melt composition to $\delta^{94}Zr_{IPGP\text{-}Zr}$ = -0.075 ‰ and Zr/Hf = 39. This fractionation model can, however, only explain a fraction of the NWA 7533 grains. The solid grey line and shaded grey field reflect the martian mantle $\delta^{94}Zr_{IPGP\text{-}Zr}$ composition (0.062 ± 0.043 ‰, Jensen *et al.*, 2025a).

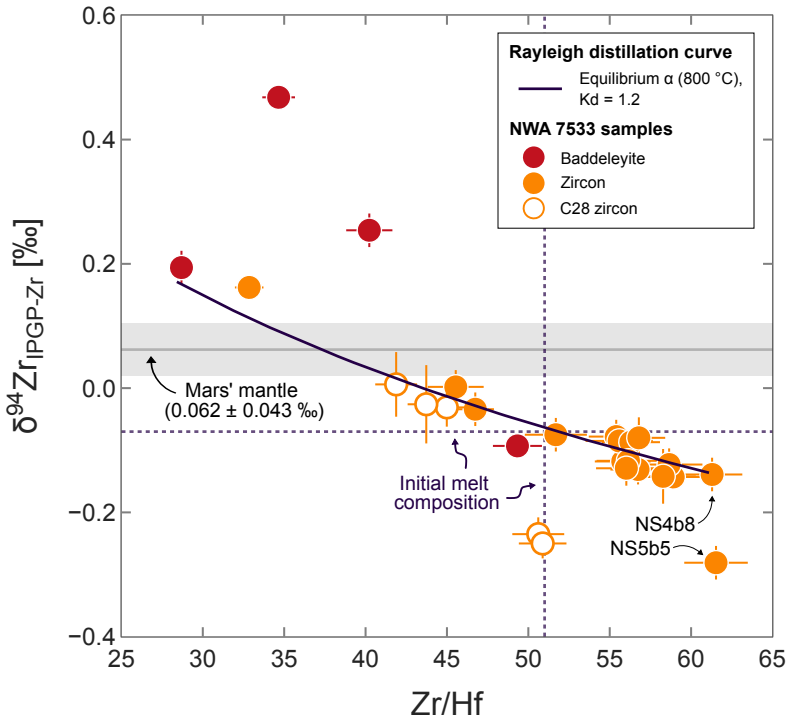


**Figure S-13** Rayleigh fractionation curve reflecting equilibrium isotope fractionation at 800 ºC (α = 0.99993) in combination with a $Kd^{Zr}/Kd^{Hf}$ value of 1.2 selected to fit the data. The dotted lines illustrate the initial melt composition used for the isotope fractionation model, and the solid grey line and shaded grey field reflect the martian mantle $\delta^{94}Zr_{IPGP\text{-}Zr}$ composition (0.062 ± 0.043 ‰, Jensen *et al.*, 2025a). The composition of a large fraction of the NWA 7533 grains can be explained by equilibrium-only isotope fractionation at 800 ºC if setting the initial melt composition to $\delta^{94}Zr_{IPGP\text{-}Zr}$ = -0.07 ‰ and Zr/Hf = 51 (and using $Kd^{Zr}/Kd^{Hf}$ = 1.2). We emphasise that this model fails to explain the grains with more extreme Zr isotope compositions, and it is assuming an initial melt composition that is significantly different from that expected based on the Zr isotope compositions measured for bulk rock samples (Jensen *et al.*, 2025a).

# Supplementary Information References

Aranovich, L.Ya., Bortnikov, N.S. (2018) New Zr–Hf Geothermometer for Magmatic Zircons. *Petrology* 26, 115–120. https://doi.org/10.1134/s0869591118020029

Blichert-Toft, J., Chauvel, C., Albarède, F. (1997) Separation of Hf and Lu for high-precision isotope analysis of rock samples by magnetic sector-multiple collector ICP-MS. *Contributions to Mineralogy and Petrology* 127, 248–260. https://doi.org/10.1007/s004100050278

Bouvier, A., Vervoort, J.D., Patchett, P.J. (2008) The Lu–Hf and Sm–Nd isotopic composition of CHUR: Constraints from unequilibrated chondrites and implications for the bulk composition of terrestrial planets. *Earth and Planetary Science Letters* 273, 48–57. https://doi.org/10.1016/j.epsl.2008.06.010

Bouvier, L.C., Costa, M.M., Connelly, J.N., Jensen, N.K., Wielandt, D., Storey, M., Nemchin, A.A., Whitehouse, M.J., Snape, J.F., Bellucci, J.J., Moynier, F., Agranier, A., Gueguen, B., Schönbächler, M., Bizzarro, M. (2018) Evidence for extremely rapid magma ocean crystallization and crust formation on Mars. *Nature* 558, 586–589. https://doi.org/10.1038/s41586-018-0222-z

Burkhardt, C., Spitzer, F., Morbidelli, A., Budde, G., Render, J.H., Kruijer, T.S., Kleine, T. (2021) Terrestrial planet formation from lost inner solar system material. *Science Advances* 7, eabj7601. https://doi.org/10.1126/sciadv.abj7601

Cavosie, A.J., Timms, N.E., Ferrière, L., Rochette, P. (2018) FRIGN zircon—The only terrestrial mineral diagnostic of high-pressure and high-temperature shock deformation. *Geology* 46, 891–894. https://doi.org/10.1130/g45079.1

Chen, X., Wang, W., Zhang, Z., Nie, N.X., Dauphas, N. (2020) Evidence from *Ab Initio* and Transport Modeling for Diffusion-Driven Zirconium Isotopic Fractionation in Igneous Rocks. *ACS Earth and Space Chemistry* 4, 1572–1595. https://doi.org/10.1021/acsearthspacechem.0c00146

Cherniak, D.J., Hanchar, J.M., Watson, E.B. (1997) Diffusion of tetravalent cations in zircon. *Contributions to Mineralogy and Petrology* 127, 383–390. https://doi.org/10.1007/s004100050287

Condon, D.J., Schoene, B., McLean, N.M., Bowring, S.A., Parrish, R.R. (2015) Metrology and traceability of U–Pb isotope dilution geochronology (EARTHTIME Tracer Calibration Part I). *Geochimica et Cosmochimica Acta* 164, 464–480. https://doi.org/10.1016/j.gca.2015.05.026

Costa, M.M., Jensen, N.K., Bouvier, L.C., Connelly, J.N., Mikouchi, T., Horstwood, M.S.A., Suuronen, J.-P., Moynier, F., Deng, Z., Agranier, A., Martin, L.A.J., Johnson, T.E., Nemchin, A.A., Bizzarro, M. (2020) The internal structure and geodynamics of Mars inferred from a 4.2-Gyr zircon record. *Proceedings of the National Academy of Sciences* 117, 30973–30979. https://doi.org/10.1073/pnas.2016326117

Creech, J.B., Paul, B. (2015) IsoSpike: Improved Double-Spike Inversion Software. *Geostandards and Geoanalytical Research* 39, 7–15. https://doi.org/10.1111/j.1751-908X.2014.00276.x

Geisler, T., Pidgeon, R.T., van Bronswijk, W., Kurtz, R. (2002) Transport of uranium, thorium, and lead in metamict zircon under low-temperature hydrothermal conditions. *Chemical Geology* 191, 141–154. https://doi.org/10.1016/S0009-2541(02)00153-5

Jensen, N.K., Deng, Z., Connelly, J.N., Bizzarro, M. (2024) Novel Methods for Concomitant Determination of the Stable Zr Isotope Composition, Lu-Hf Isotope Systematics and U-Pb Age of Individual Zircons. *Geostandards and Geoanalytical Research* 48, 5–28. https://doi.org/10.1111/ggr.12529

Jensen, N.K., Deng, Z., Bizzarro, M. (2025a) The stable Zr isotope composition of the martian mantle. *Chemical Geology* 688, 122811. https://doi.org/10.1016/j.chemgeo.2025.122811

Jensen, N.K., Nemchin, A.A., Kenny, G., Whitehouse, M.J., Connelly, J.N., Mikouchi, T., Bizzarro, M. (2025b) Timing of crustal reworking on Mars inferred from the Lu-Hf isotope systematics of igneous clasts in NWA 7533. *Geochimica et Cosmochimica Acta* 390, 70–85. https://doi.org/10.1016/j.gca.2024.11.014

Jiang, S.-Y., Wang, R.-C., Xu, X.-S., Zhao, K.-D. (2005) Mobility of high field strength elements (HFSE) in magmatic-, metamorphic-, and submarine-hydrothermal systems. *Physics and Chemistry of the Earth, Parts A/B/C* 30, 1020–1029. https://doi.org/10.1016/j.pce.2004.11.004

Krogh, T.E. (1973) A low-contamination method for hydrothermal decomposition of zircon and extraction of U and Pb for isotopic age determintations. *Geochimica et Cosmochimica Acta* 37, 485–494. https://doi.org/10.1016/0016-7037(73)90213-5

McLean, N.M., Condon, D.J., Schoene, B., Bowring, S.A. (2015) Evaluating uncertainties in the calibration of isotopic reference materials and multi-element isotopic tracers (EARTHTIME Tracer Calibration Part II). *Geochimica et Cosmochimica Acta* 164, 481–501. https://doi.org/10.1016/j.gca.2015.02.040

Patchett, P.J., Tatsumoto, M. (1980) Lu–Hf total-rock isochron for the eucrite meteorites. *Nature* 288, 571–574. https://doi.org/10.1038/288571a0

Paton, C., Hellstrom, J., Paul, B., Woodhead, J., Hergt, J. (2011) Iolite: Freeware for the visualisation and processing of mass spectrometric data. *Journal of Analytical Atomic Spectrometry* 26, 2508–2518. https://doi.org/10.1039/c1ja10172b

Render, J., Brennecka, G.A., Burkhardt, C., Kleine, T. (2022) Solar System evolution and terrestrial planet accretion determined by Zr isotopic signatures of meteorites. *Earth and Planetary Science Letters* 595, 117748. https://doi.org/10.1016/j.epsl.2022.117748

Rubatto, D. (2002) Zircon trace element geochemistry: partitioning with garnet and the link between U–Pb ages and metamorphism. *Chemical Geology* 184, 123–138. https://doi.org/10.1016/S0009-2541(01)00355-2

Russell, W.A., Papanastassiou, D.A., Tombrello, T.A. (1978) Ca isotope fractionation on the Earth and other solar system materials. *Geochimica et Cosmochimica Acta* 42, 1075–1090. https://doi.org/10.1016/0016-7037(78)90105-9

Söderlund, U., Patchett, P.J., Vervoort, J.D., Isachsen, C.E. (2004) The $^{176}$Lu decay constant determined by Lu–Hf and U–Pb isotope systematics of Precambrian mafic intrusions. *Earth and Planetary Science Letters* 219, 311–324. https://doi.org/10.1016/s0012-821x(04)00012-3

Steiger, R.H., Jäger, E. (1977) Subcommission on geochronology: Convention on the use of decay constants in geo- and cosmochronology. *Earth and Planetary Science Letters* 36, 359–362. https://doi.org/10.1016/0012-821X(77)90060-7

Stevenson, R.K., Patchett, P.J. (1990) Implications for the evolution of continental crust from Hf isotope systematics of Archean detrital zircons. *Geochimica et Cosmochimica Acta* 54, 1683–1697. https://doi.org/10.1016/0016-7037(90)90400-F

Tian, S., Moynier, F., Inglis, E.C., Jensen, N.K., Deng, Z., Schiller, M., Bizzarro, M. (2022) Determination of the zirconium isotopic composition of the new isotopic standard NRC ZIRC-1 using MC-ICP-MS. *Journal of Analytical Atomic Spectrometry* 37, 656–662. https://doi.org/10.1039/d1ja00418b

Tissot, F.L.H., Ibañez-Mejia, M., Rabb, S.A., Kraft, R.A., Vocke, R.D., Fehr, M.A., Schönbächler, M., Tang, H., Young, E.D. (2023) A community-led calibration of the Zr isotope reference materials: NIST candidate RM 8299 and SRM 3169. *Journal of Analytical Atomic Spectrometry* 38, 2087–2104. https://doi.org/10.1039/D3JA00167A

Vervoort, J.D., Blichert-Toft, J. (1999) Evolution of the depleted mantle: Hf isotope evidence from juvenile rocks through time. *Geochimica et Cosmochimica Acta* 63, 533–556. https://doi.org/10.1016/S0016-7037(98)00274-9